

Effect of Alloying Elements on the Microstructure and Corrosion Resistance of Zn–5Al–2Mg Alloy

Wenxuan Chen^a, Huijie Sun^a, Guorong Zhou^{a, *}, Xuefeng Wang^a, and Degang Zhao^a

^a School of Materials Science and Engineering, University of Jinan, Jinan, 250022 China

*e-mail: mse_zhougr@ujn.edu.cn

Received May 5, 2022; revised July 12, 2022; accepted August 10, 2022

Abstract—Zn–Al–Mg alloys with the alloying elements of Si, Ti and Zr by microalloying method were designed. The microstructure was well characterized, and the Rockwell hardness as well as anti-corrosion were tested. The results showed that the alloys with Si, Ti and Zr elements not only contain the same Al rich phase, Zn rich phase and lamellar Zn/Al/MgZn₂ ternary eutectic structure as Zn–5Al–2Mg, but also the formation of Si rich phase, Ti(Al_{1-x}Si_x)₃ phase, Al₃Zr phase and Al₃(Ti, Zr) phase, respectively. The electrochemical test demonstrated that Zn–5Al–2Mg–0.2(TiZr) alloy has higher corrosion resistance as compared to that with the addition of (Si,Ti) and (Si,Zr) elements. Therefore, the addition of Ti and Zr elements can greatly improve the corrosion resistance of Zn–5Al–2Mg alloy. Moreover, the corrosion products of Zn–5Al–2Mg alloy and Zn–5Al–2Mg–0.2(TiZr) alloy were tested by XPS. The results showed that the addition of Ti and Zr inhibits the formation of loose porous ZnO, while promotes the formation of compact Zn₅(CO₃)₂(OH)₆, Zn₃(CO₃)₂(OH)₆ can adhere to the sample surface well, hinder the charge transfer, and improve the corrosion resistance of the alloy.

Keywords: Zn–5Al–2Mg alloy, microstructure, corrosion resistance, grain refinement

DOI: 10.1134/S2070205122060041

1. INTRODUCTION

Steel is widely used in building, automobiles, appliances and construction industry due to its high strength, good processing performance and low production cost [1–3]. However, steel is prone to corrosion, which has brought great losses to the national economy [4]. Hot-dip zinc coating can provide not only the barrier protection but also the galvanic protection to the steel substrate. With the further development of modern industry, traditional hot-dip galvanizing can no longer meet the demand for corrosion resistance [5, 6]. Recently, researchers have found that Zn–Al–Mg alloys have better corrosion resistance than traditional zinc coatings and Zn–Al alloys, so Zn–Al–Mg alloys have been extensively studied [7, 8]. For example, the corrosion resistance of Zn–6Al–3Mg alloy produced by Nisshin Steel Group is nearly 10 times higher than that of traditional galvanized sheet, and it is widely used in construction, automobile industries and so on [9, 10].

By adding other elements (such as Si, Ti, Zr, Re, etc.) to further improve the corrosion resistance of Zn–Al–Mg alloys. Li et al. [11] analyzed the effects of Re and Si on the microstructure and corrosion resistance of Zn–6Al–3Mg hot dip coating. The results indicated that the additions of Si and Re suppress the intergranular corrosion and pitting that occurred in

the Zn–6Al–3Mg coating. Thereby, the corrosion resistance of Zn–6Al–3Mg alloy is improved. Zn–11Al–3Mg–0.2Si alloy designed by Nippon Steel has a series of advantages of super corrosion resistance, excellent black denaturation resistance and good formability. It is mainly used in household appliance industry [12, 13]. In addition, by adding proper amounts of Ti to the Zn–Al–Mg alloy, Ti can be used as heterogeneous nucleation particles to refine the alloy structure. The addition of Ti form a stable, strong bonding, protective and dense oxide film on the surface of the alloy coating to improve the corrosion resistance of the alloy [14, 15]. Xu et al. [16] studied the microstructure and properties of a new Al–Cu–Mg–Zn–Zr–Ti heat resistant aluminum alloy. It was found that the alloy with Ti added has good resistance to intergranular corrosion. Liu et al. [17] analyzed the effect of Ti addition on microstructure and corrosion property of Zn–5Al alloy. The results showed that a small amount of Ti addition in Zn–5Al alloy refines the primary Zn phase and increases the percentage of the eutectic structure, and finally improves the corrosion resistance of Zn–5Al alloy. Moreover, researchers have also found that adding an appropriate amount of Zr can improve the anti-corrosion characters of the alloy. Chai et al. [18] studied the effect of minor Zr addition on exfoliation corrosion resistance Al–Zn–Mg–Mn alloy sheet. The results showed that the exfo-

Table 1. The elemental composition of alloys

Sample	Element, wt %					
	Al	Mg	Si	Ti	Zr	Zn
Zn–5Al–2Mg	5	2	/	/	/	Bal.
Zn–5Al–2Mg–0.1(SiTi)	5	2	0.1	0.1	/	Bal.
Zn–5Al–2Mg–0.1(SiZr)	5	2	0.1	/	0.1	Bal.
Zn–5Al–2Mg–0.1(TiZr)	5	2	/	0.1	0.1	Bal.
Zn–5Al–2Mg–0.2(SiTi)	5	2	0.2	0.2	/	Bal.
Zn–5Al–2Mg–0.2(SiZr)	5	2	0.2	/	0.2	Bal.
Zn–5Al–2Mg–0.2(TiZr)	5	2	/	0.2	0.2	Bal.

liation corrosion resistance of Al–Zn–Mg–Mn alloy sheet was significantly improved due to the addition of Zr. Zhou et al. [19] studied the effect of Zr content on microstructure and corrosion resistance of hot-dip galvanized Zn–0.1% Ni–Zr alloy. It can be found that the electrochemical impedance and polarization resistance of Zn–0.1% Ni–Zr alloy are increased, and then improve the corrosion resistance of the alloy.

Moreover, in the previous works, most researchers paid more attention to the effect of single element addition on the corrosion resistance of Zn–5Al–2Mg alloy. Few people have studied adding two elements with equal proportions to Zn–Al–Mg alloy. In this work, the effect of (Si, Ti), (Si, Zr) and (Ti, Zr) elements with equal proportions on the microstructures and corrosion resistance of Zn–5Al–2Mg alloy was studied.

2. EXPERIMENTAL

The alloy raw materials used in the experiment were Zn (99.99 wt %), pure Mg (99.95 wt %), pure Al (99.95 wt %) and Al–20Si, Al–10Zr, Mg–30Zr and Al–5Ti master alloys. Zn–5Al–2Mg– x (SiTi), Zn–5Al–2Mg– y (SiZr) and Zn–5Al–2Mg– z (TiZr) ($x = y = z = 0, 0.1, 0.2$) (wt %, same below) alloy were melted within a crucible in resistance furnace. Set the temperature of the resistance furnace to 720°C, added the treated alloy ingot, heated them to complete melting. Then set the furnace temperature to 550°C and kept at this temperature for a certain time. Finally, stirred evenly, and cast into the mold under atmospheric conditions to obtain the alloy ingot required for the experiment. The alloy elemental composition was shown in Table 1.

Alloy microstructures were studied after grinding and polishing by scanning electron microscopy (SEM; FEG-250) with back scattered electron (BSE) imaging. While the phase composition was analysed by X-ray diffraction spectrometry (XRD; D8-advanY) and energy dispersive X-ray spectrometry (EDS), respectively. The ingot was cut into thin pieces, 0.3 mm thick, by electrospark. Sample preparations for TEM (JEM-2100) with EDS observation included

mechanical polishing and ion-beam thinning (GATAN-691). In addition, the hardness of alloy samples was measured by the Rockwell hardness tester (HBRV-187.5).

All the electrochemical tests were carried out using IM6d Zahner-Elektrik workstation at room temperature. A standard three-electrode system was used to test samples. Standard saturated calomel electrode (SCE) was used as reference electrode, metal platinum electrode as the counter electrode and the sample with a test surface of 1 cm² as the working electrode. The samples were subjected to dynamic polarization after stabilizing the open circuit potential (OCP) for 30 min in all the experiments. Electrochemical impedance spectra (EIS) were performed under the sinusoidal potential perturbation of ± 10 mV after stabilizing the open circuit potential in the frequency range of $10^{-1} \sim 10^5$ Hz. Polarization curves were recorded at the voltage range of -2 to 0 V and the scanning rate of the polarization curve was 10 mV/s. The corroding medium of all electrochemical tests was 3.5% NaCl solution. Besides, in order to further test the corrosion resistance of alloy samples, total immersion weight loss method was carried out. The weight loss of the samples was gravimetrically calculated by measuring the weight difference before and after removing the corrosion products by chemical cleaning in NH₄Cl solution according to GB/T16545-1996. Immersed the test surface with 1 cm² in 3.5% NaCl solution, every three days as a cycle, 7 cycles in total. The corrosion products of the alloy samples were analyzed by X-ray photoelectron spectroscopy (XPS) of Thermo Fisher Scientific ESCALAB Xi+.

3. RESULTS AND DISCUSSION

3.1. Microstructure and Phase Constituent of Zn–Al–Mg Alloys

In order to identify the phase composition of alloy samples, XRD of four Zn–Al–Mg alloys were tested. The results were presented in Fig. 1. As can be seen from the results, that Zn, Al and MgZn₂ phases were identified in all alloys. However, the diffraction peaks

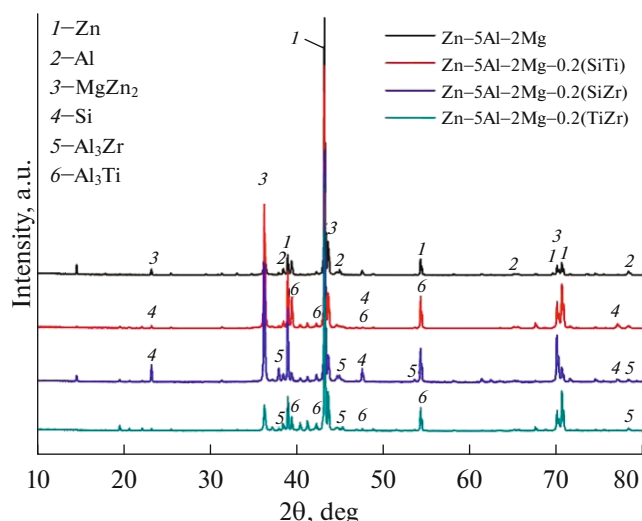


Fig. 1. XRD spectrum of Zn–5Al–2Mg and Zn–5Al–2Mg–0.2(Si/Ti/Zr) alloys.

of Si-rich phase, Al_3Ti phase and Al_3Zr phase appeared in the alloy samples, by adding Si, Ti and Zr in binary and equal proportion, respectively [17, 18]. In addition, it is not enough to meet the conditions of phase quantitative analysis by XRD because the sample was as-cast and had a strong preferred orientation.

The surface microstructure and phase composition of the alloys were analysed using SEM and EDS. As showed in Fig. 2, it is clearly observed that the typical structure of Zn–5Al–2Mg alloy consisted of the black Al phase, the white Zn phase attached around the Al phase dendrite, and lamellar Zn/Al/MgZn₂ ternary eutectic structure. In Fig. 3, the microstructure of six alloys (Zn–5Al–2Mg–0.1/0.2(SiTi), Zn–5Al–2Mg–0.1/0.2(SiZr) and Zn–5Al–2Mg–0.1/0.2(TiZr)) was studied. Firstly, as indicated in Figs. 3a, 3b, the Al dendrite arm was greatly short and Zn dendrite was slightly increased by adding Si and Ti elements. In addition, it can be found that when the addition of (Si, Ti)

was 0.2 wt %, the lamellar spacing of ternary eutectic structure increased obviously. Secondly, as can be seen in Figs. 3c, 3d, the size of Al dendrites had not obviously changed with the addition of (Si, Zr) element. However, the percentage of Zn rich phase increased and the lamellar spacing of ternary eutectic structure also increased with the increasing of (Si, Zr) element. Finally, it is indicated that Al and Zn dendrites decreased with the increasing of (Ti, Zr) element addition in Figs. 3e, 3f. Nevertheless, compared with that of Zn–5Al–2Mg alloy, the lamellar spacing of ternary eutectic structure of Zn–5Al–2Mg–0.1/0.2(TiZr) alloys first increased and then decreased with the increase of addition. In particular, it is worth noticing that the Zn–5Al–2Mg–0.2(TiZr) alloy had the shortest dendrite arm and the largest percentage of ternary eutectic structure among them.

Zn–5Al–2Mg–0.2(SiTi), Zn–5Al–2Mg–0.2(SiZr) and Zn–5Al–2Mg–0.2(TiZr) alloys were selected to test EDS. The selected points were marked in Fig. 4, and the results of point analysis were listed in Table 2. According to the results of point analysis, it can be found that the percentages of Si atoms at points 1 and 4 were 93.17 and 81.47%, respectively, which corresponded to the Si rich phase. However, Point 2 was located at the black block phase in Fig. 4a, and the ratio of Ti and (Al,Si) was closed to 1 : 3, which was considered as the $\text{Ti}(\text{Al}_{1-x}\text{Si}_x)_3$ phase. $\text{Ti}(\text{Al}_{1-x}\text{Si}_x)_3$ phase still maintained the crystal structure of Al_3Ti phase. Due to the atomic radius of Al and Si were similar, Si atom can replaced Al ions in the lattice structure of Al_3Ti phase to form $\text{Ti}(\text{Al}_{1-x}\text{Si}_x)_3$ phase [20]. At point 5, it showed that the primary Al phase contained up to 53% Zn, because compositional segregation occurred in the Al-rich phase during solidification. The point analysis results of the eutectic region of the alloy structures at points 6 and 8 were very closed to the atomic ratio of MgZn_2 phase, and the content of Al element in the eutectic region was low. It is indicated that there should be coexistence of Zn and MgZn_2 phases here [21]. The ratio of Al and (Ti, Zr)

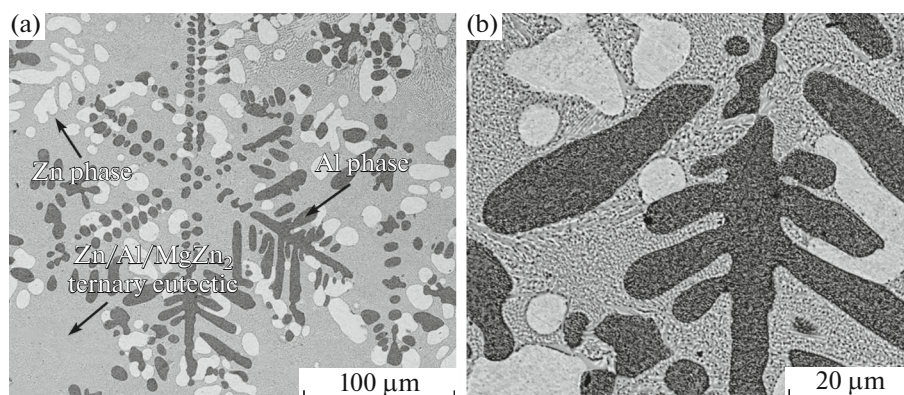


Fig. 2. The SEM image of Zn–5Al–2Mg alloy.

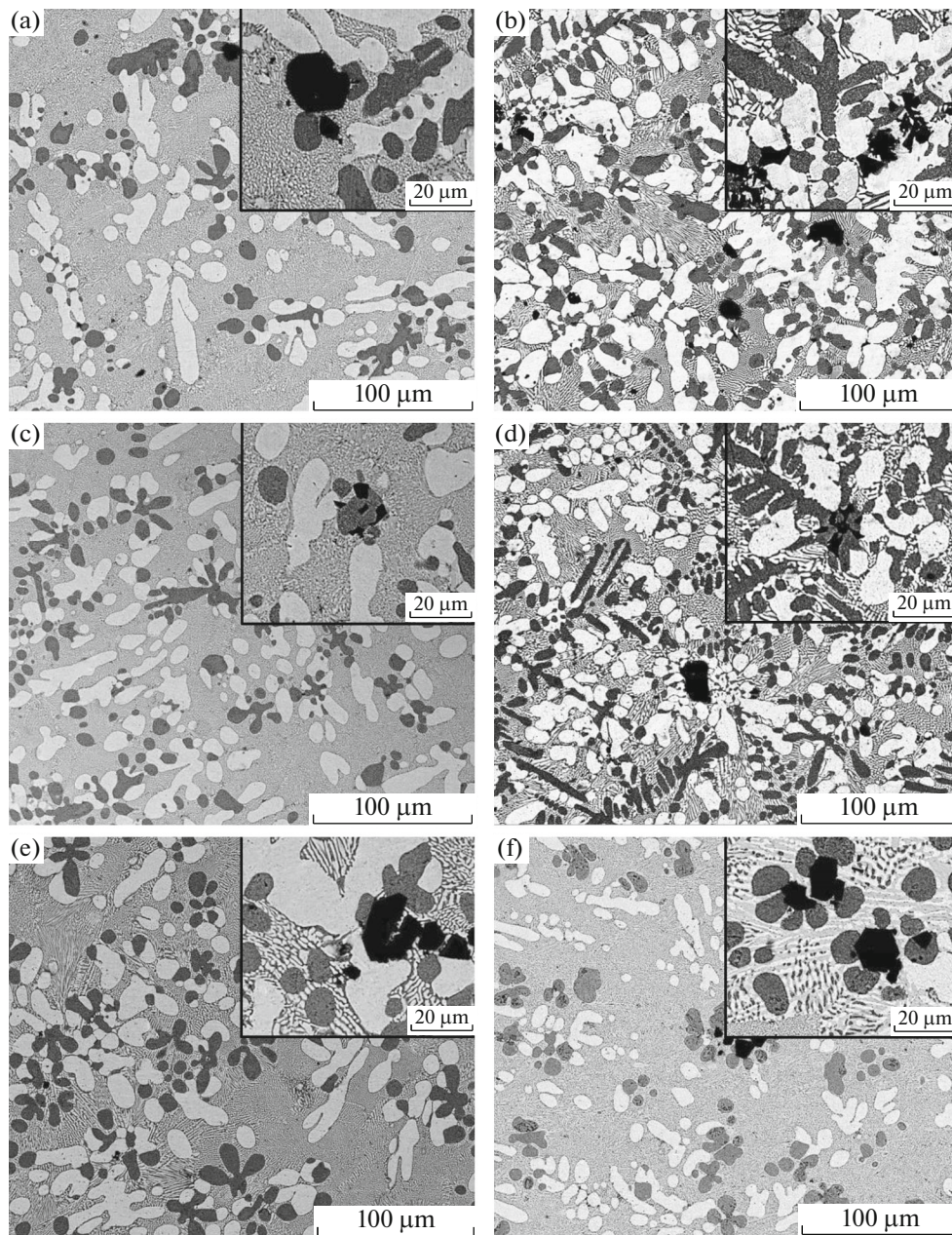


Fig. 3. SEM images of Zn–5Al–2Mg– x (SiTi), Zn–5Al–2Mg– y (SiZr) and Zn–5Al–2Mg– z (TiZr) alloys: (a, c, e,) $x = y = z = 0.1$; (b, d, f) $x = y = z = 0.2$.

was close to 3 : 1 at point 7, which was supposed to $\text{Al}_3(\text{Ti}, \text{Zr})$ phase. Owing to the Al_3Zr phase will precipitated preferentially with the addition of Ti and Zr elements when the temperature was above the peritectic reaction temperature of Al–Ti. When Al_3Zr just precipitated and not aggregated, the Ti atom can replaced the Zr atom in Al_3Zr to form the $\text{Al}_3(\text{Ti}_x\text{Zr}_{1-x})$ phase [22]. At the same time, combined with Table 2, it can be known that this was the coexistence of Zn, Al and MgZn_2 phases at points 3 and 9 in Fig. 4.

In order to determine the phase composition of the ternary eutectic structure in the alloy more accurately, Zn–5Al–2Mg–0.1(SiTi) alloy was detected by TEM and EDS. The bright-field phase of the Zn–5Al–2Mg–0.1(SiTi) alloy was showed in Figs. 5a, 5d, 5g. Figs. 5b, 5c, 5e, 5h, 5f, 5i were respectively the selected area electron diffraction and energy-dispersive spectroscopy analysis corresponding to Figs. 5a, 5d, 5g. Through the bright field phase and the SAED pattern in Figs. 5a, 5b, it is determined that there was an Al phase in the eutectic region of the alloy, which corre-

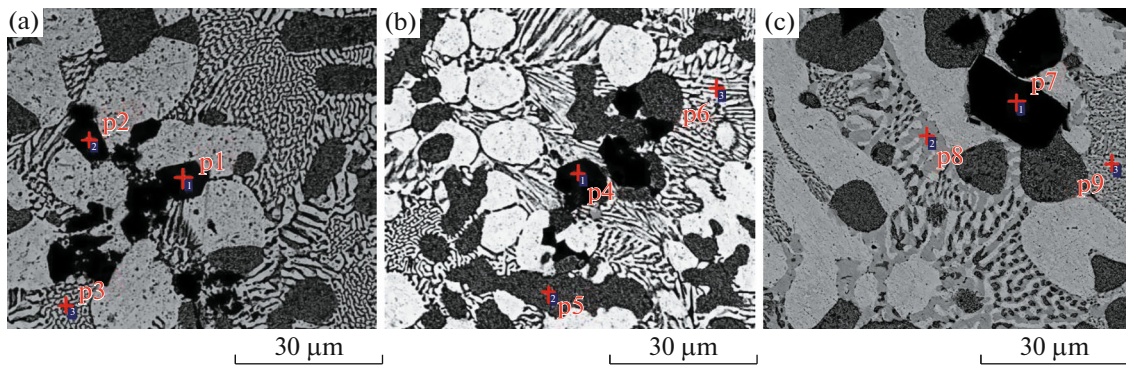


Fig. 4. EDS spectra of alloys: (a) Zn-5Al-2Mg-0.2(SiTi); (b) Zn-5Al-2Mg-0.2(SiZr); (c) Zn-5Al-2Mg-0.2(TiZr).

sponded to the result of EDS analysis. Besides, the phase was indexed as $[\bar{1}\bar{1}\bar{1}]Al$, so the particle was identified to be fcc-Al. According to the SAED pattern (Fig. 5e) and the result of EDS analysis (Fig. 5f), this phase was considered to be $[\bar{1}101]Zn$. There were two forms of Zn in the eutectic structure, lamellar Zn and Zn particles wrapped in Al ring, showing in Fig. 6. In Fig. 5i, it can be seen that the ratio was very closed to the atomic ratio of $MgZn_2$, and the SAED pattern (Fig. 5h) was consistent with $[\bar{1}\bar{2}\bar{1}\bar{3}]MgZn_2$. Therefore, the ternary eutectic structure was composed of Al, Zn and $MgZn_2$ phase.

3.2. Rockwell Hardness

The addition of Si, Ti and Zr elements to the Zn-5Al-2Mg alloy contributed to a substantial increase in Rockwell hardness values as compared to the Zn-5Al-2Mg alloy, as showed in Fig. 7. It is clearly observed that with the increase of the addition of (Si, Ti) and (Si, Zr), the hardness values of the alloys first increased and then decreased, and the maximum values were 79.95 HRB and 72.03 HRB, respectively. However, the hardness value of Zn-5Al-2Mg-z(TiZr) alloy was increasing all the time. The Rockwell hardness value of Zn-5Al-2Mg-z(TiZr) alloy reached the maximum value of 77.79 HRB by the content of the addition (Ti, Zr) reached to 0.2 wt %. Combined with the analysis of microstructure, the hardness value was improved for the following reasons: (1) The structure of the alloy was refined by the addition of Si, Ti and Zr elements. According to the fine grain strengthening theory, the more the number of grains, the finer the grains, and the plastic deformation caused by external force can be dispersed in more grains. The plastic deformation was more uniform and the stress concentration was smaller, so the alloy sample had higher hardness. (2) The thickness of the Zn/Al/ $MgZn_2$ ternary eutectic structure played a significant role in the crack resistance and comprehensive mechanical properties of the galvanized alloy [23]. Combined with the appeal analyses, adding an appropriate amount of Si, Ti and Zr elements to Zn-5Al-

2Mg alloy could improve the hardness value of the alloy.

3.3. Electrochemical Impedance Spectroscopy (EIS)

Changed in OCP values as a function of immersion time were monitored for all the alloys in 3.5 wt % NaCl solution and the results were given in Fig. 8. The change of OCP at different immersion periods, showed a continuous change in the morphology of metal surfaces and corrosion products [24]. As reported in [25, 26], a relatively stable OCP value indicated a stable state between the advance of corrosion and the deposition of corrosion products. These samples exhibited a similar tendency with the immersion time, indicating that all alloys experienced a similar corrosion process. In addition, the curve of the open potential gradually tended to be stable after 1500 s.

The EIS spectra of Zn-5Al-2Mg-x(SiTi), Zn-5Al-2Mg-y(SiZr), Zn-5Al-2Mg-z(TiZr) alloys were tested in the frequency range of 10^{-1} - 10^5 Hz, showed in Fig. 9. As seen in Figs. 9a, 9d, the Nyquist plots were composed of two capacitive loops: high frequency and low frequency, indicating the existence of two time constants. The first time constant at high fre-

Table 2. The EDS results at the point in Fig. 4

Point	Element, at %					
	Zn	Al	Mg	Si	Ti	Zr
1	3.57	2.95	0.31	93.17		
2	3.82	5.10	0.18	65.99	24.91	
3	78.65	10.20	11.16			
4	6.56	8.37	0.46	81.47		3.14
5	53	47				
6	73	2.51	24.49			
7	21.43	53.90			22.65	2.02
8	78.5	2.88	18.62			
9	76.38	18.81	4.82			

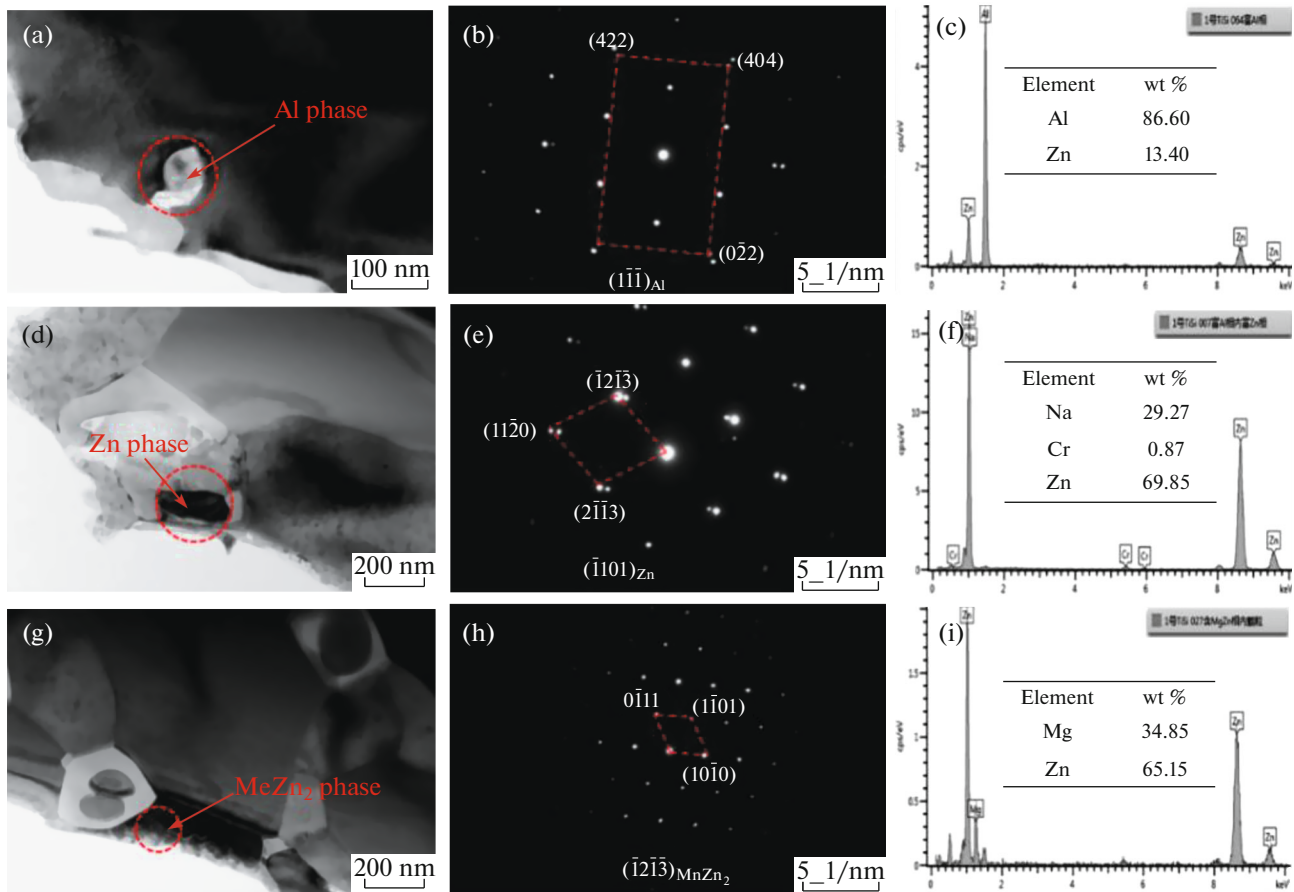


Fig. 5. The TEM analyses of ternary eutectic structure in Zn–5Al–2Mg–0.1(SiTi) alloy: (a, d, g) bright field phases, (b, e, h) diffraction patterns and (c, f, i) energy-dispersive spectroscopy analyses.

quency was attributed to electrolyte penetration including water uptake and salt intrusion, and the second time constant at low frequency was related to the charge transfer of the corrosion process [27, 28]. Moreover, the larger the diameter of the semi-circle is, the higher the resistance is and the lower the corrosion

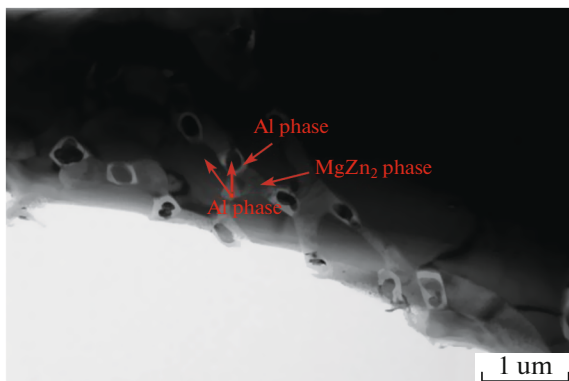


Fig. 6. TEM image of Zn/Al/MgZn₂ ternary eutectic structure.

rate is [29]. It is clear that all these alloy samples had exhibited significantly higher charge transfer resistance than the Zn–5Al–2Mg alloy, besides, the Zn–5Al–2Mg–0.1(SiTi) alloy. B-P diagrams (Bode phase angle curve) in Figs. 9b, 9e and B-|Z| diagrams (Amplitude-frequency characteristic curve) in Figs. 9c, 9f were plotted and compared. Figs. 9b, 9e showed the wave crest at a frequency around the range of 10^2 – 10^3 Hz for tested specimens. Based on the observation of Bode impedance |Z| diagrams in Figs. 9c, 9f, it is interesting to notice that the |Z| value of Zn–5Al–2Mg alloy was improved with the addition of Si, Ti and Zr, indicating that improved the corrosion resistance of Zn–5Al–2Mg alloy. However, the |Z| value and the semi-circle diameter of Zn–5Al–2Mg–0.1(SiTi) alloy were slightly lower than that of Zn–5Al–2Mg alloy, the result showed that when the content of Si and Ti was 0.1 wt %, the resistance of the alloy to corrosive medium was weakened and the corrosion resistance of the alloy was reduced at the initial stage of corrosion.

An equivalent electrical circuit (EEC), used to fit the experimental data was given in Fig. 10. R_s repre-

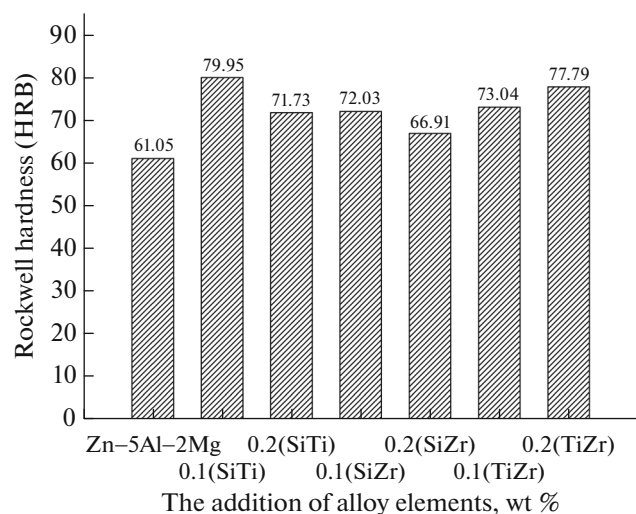


Fig. 7. The Rockwell hardness diagram of Zn-5Al-2Mg- x (SiTi), Zn-5Al-2Mg- y (SiZr) and Zn-5Al-2Mg- z (TiZr) alloys.

sented the solution resistance, R_f represented the resistance of the corrosion product layer, R_{ct} was the charge transfer resistance, Q_1 and Q_2 were constant phase angle elements of corrosion product layer and electric double layer capacitance, respectively; n represented the dispersion coefficient, and the dimensionless constant range was 0–1 [30]. For $n = 1$, the constant phase element represented a pure capacitor, $n = 0$ repre-

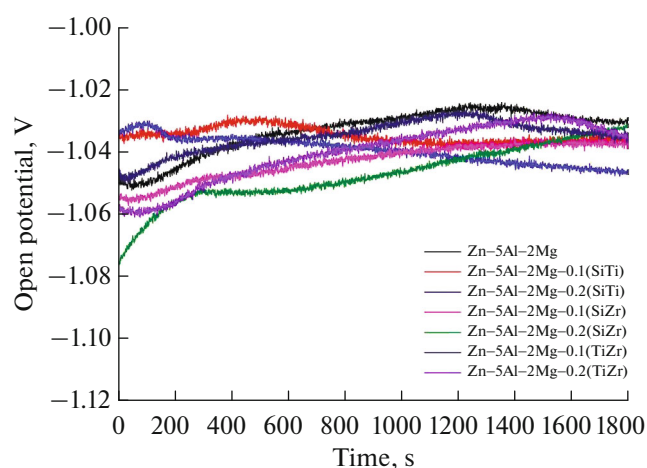


Fig. 8. Change in OCP values of cast alloys as a function of time in 3.5 wt % NaCl solution.

sented a pure resistor, and $n = 0.5$ was a Warburg impedance with a diffusion character [31, 32].

The fitted EIS parameters were summarized in Table 3. As compared in Table 3, the R_s of all tests were much lower than R_f and R_{ct} , indicating that all tests were in a stable environment. The EEC model did not change after adding Si, Ti and Zr, showing that the corrosion behaviour of the Zn-5Al-2Mg alloy did not change at the initial stage of corrosion. Independent of the proposed EEC model, the corrosion performance of the samples can be characterized by con-

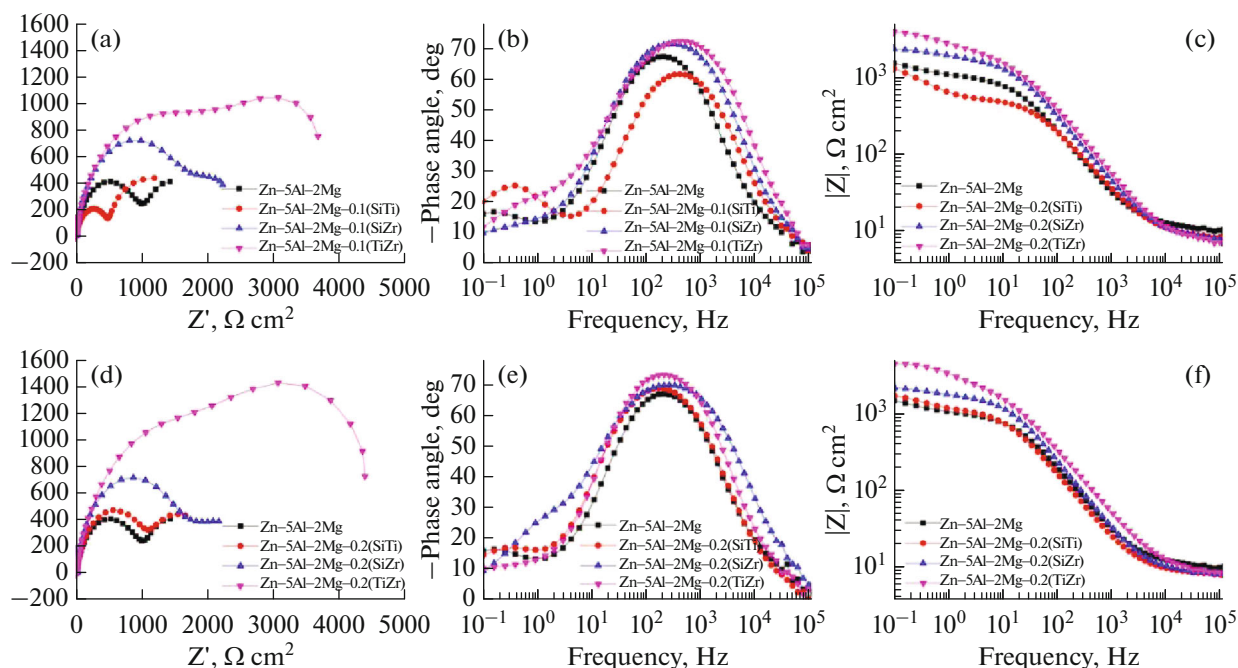


Fig. 9. EIS spectra of alloys in 3.5 wt % NaCl solution: (a, d) Nyquist diagrams; (b, e) Bode phase angle diagrams and (c, f) Bode impedance $|Z|$ diagrams.

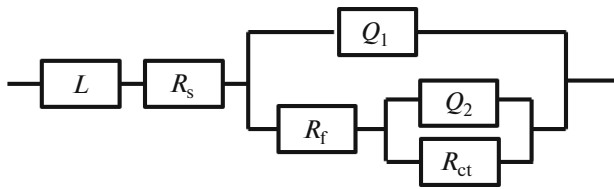


Fig. 10. Equivalent circuit model for EIS data fitting of the experimental materials.

sidering the value of R_p [33]. The value of polarization resistance R_p was equal to the resistance of the corrosion product layer R_f plus the charge transfer resistance R_{ct} [34]. In principle, R_p can be considered as being inversely proportional to the corrosion rate, the greater the polarization resistance, the smaller the corrosion rate [28]. The R_p of the alloys by adding to Ti and Zr elements were much higher than Zn–5Al–2Mg alloy, demonstrating that the addition of Ti and Zr greatly reduced the corrosion rate of the alloy. The reason was that Ti and Zr elements, as commonly used refiners in Al alloy, had good grain refining effect. Ti and Zr elements were inherently good corrosion resistance. Hence, the addition of Ti and Zr could significantly improve the corrosion resistance of the Zn–5Al–2Mg alloy, making corrosion difficult to occur.

3.4. Potentiodynamic Polarization

The polarization curve tests were conducted in 3.5 wt % NaCl solution, and corresponding plots were shown in Fig. 11. The corrosion potential (E_{corr}) and corrosion current density (I_{corr}) had been estimated using Tafel extrapolation, and obtained values were listed in Table 4. In Fig. 11, The E_{corr} of these alloys by addition to (Si, Ti), (Si, Zr) and (Ti, Zr) were more higher than for Zn–5Al–2Mg alloy, indicating that the addition of (Si, Ti), (Si, Zr) and (Ti, Zr) made the alloy more difficult to corrosion. The E_{corr} and I_{corr} of

Zn–5Al–2Mg and Zn–5Al–2Mg–0.2(TiZr) alloys were -1.526 V and $2.461 \text{ E-}4 \text{ A/cm}^2$, -1.416 V and $1.176 \text{ E-}4 \text{ A/cm}^2$ in Table 4, respectively. The E_{corr} and I_{corr} of Zn–5Al–2Mg–0.2(TiZr) alloy increased by 0.110 V and decreased by 52.21% compared with Zn–5Al–2Mg alloy separately. Hence, the addition of Ti and Zr elements significantly increased corrosion resistance of the alloy. The reason was that the microstructure uniformity of Zn–5Al–2Mg–0.2(TiZr) alloy was improved and the lamellar spacing of ternary eutectic structure was reduced. A dense corrosion product layer was formed at the initial stage of corrosion, which hinders further the diffusion of corrosion ions. Relevant studies also showed that [35] the dense Zn/Al/MgZn₂ ternary eutectic structure reduced the possibility of intergranular corrosion and improved the corrosion resistance of the alloy.

3.5. Total Immersion Test

The total immersion test was regarded as one of the most accurate methods to characterize the corrosion rate. The corrosion rate was calculated based on mass loss of all alloys immersed in 3.5 wt % NaCl solution, and the results were plotted in Fig. 12. In Fig. 12a, all the curves showed similar characteristic, with the immersion time increased, the corrosion rate first increased slowly, then decreased, then increased sharply and then decreased, and finally showed a slow rising trend. It is obvious that the corrosion rate was the highest on the 15th day. The Average corrosion rate histogram of alloys was showed in Fig. 12b. The corrosion rate of all alloys was lower than Zn–5Al–2Mg alloy, and the order was Zn–5Al–2Mg > Zn–5Al–2Mg–(SiTi) > Zn–5Al–2Mg–(SiZr) > Zn–5Al–2Mg–(TiZr). It is clearly observed that the corrosion rate of Zn–5Al–2Mg–0.2(TiZr) alloy was the lowest in these alloys, including that the corrosion resistance of Zn–5Al–2Mg–0.2(TiZr) alloy was best. This result was in line with the above EIS results, demonstrating fur-

Table 3. Equivalent circuit parameters obtained via fitting the EIS data results of alloys

Sample	Parameter							R_p , $\Omega \text{ cm}^2$
	R_s , $\Omega \text{ cm}^2$	Q_1 , $\Omega^{-1} \text{ s}^n \text{ cm}^{-2}$	n_1	R_f , $\Omega \text{ cm}^2$	Q_2 , $\Omega^{-1} \text{ s}^n \text{ cm}^{-2}$	n_2	R_{ct} , $\Omega \text{ cm}^2$	
Zn–5Al–2Mg	10.35	$1.979 \text{ E-}5$	0.856	1007	$1.591 \text{ E-}3$	0.7352	1344	2351
0.1(SiTi)	8.043	$2.179 \text{ E-}5$	0.8274	522.1	$9.322 \text{ E-}4$	0.8597	1053	1575.1
0.1(SiZr)	9.181	$9.369 \text{ E-}6$	0.8982	2132	$3.651 \text{ E-}4$	0.5343	2368	4500
0.1(TiZr)	7.097	$8.701 \text{ E-}6$	0.8756	1635	$2.16 \text{ E-}4$	0.4975	3804	5439
0.2(SiTi)	8.348	$2.272 \text{ E-}5$	0.8652	1129	$1.122 \text{ E-}3$	0.7608	1208	2337
0.2(SiZr)	8.515	$1.27 \text{ E-}5$	0.8951	1651	$1.171 \text{ E-}3$	0.6137	1386	3037
0.2(TiZr)	8.449	$1.278 \text{ E-}5$	0.8412	2560	$1.286 \text{ E-}4$	0.7683	2560	5120

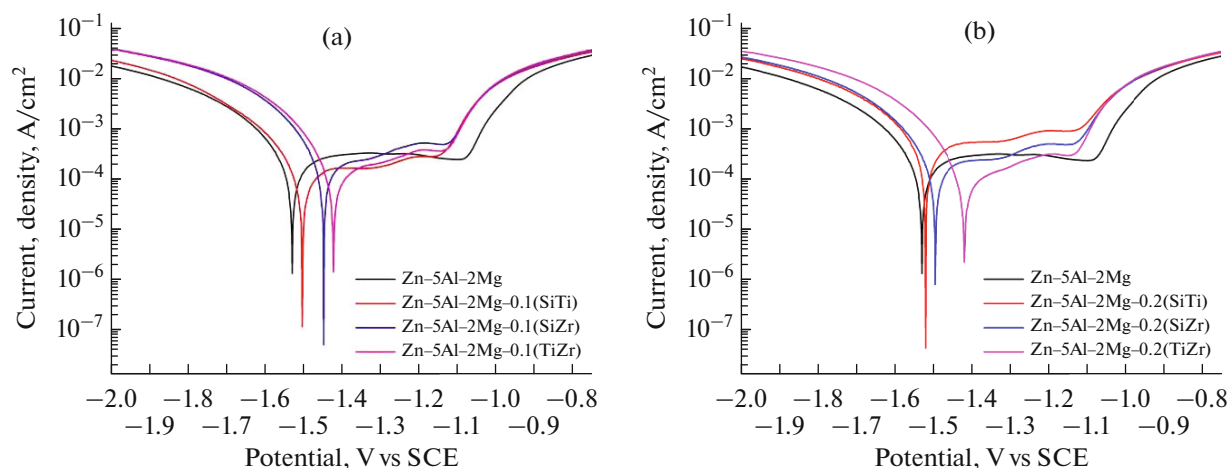


Fig. 11. Polarization curves of alloys in 3.5 wt % NaCl solution.

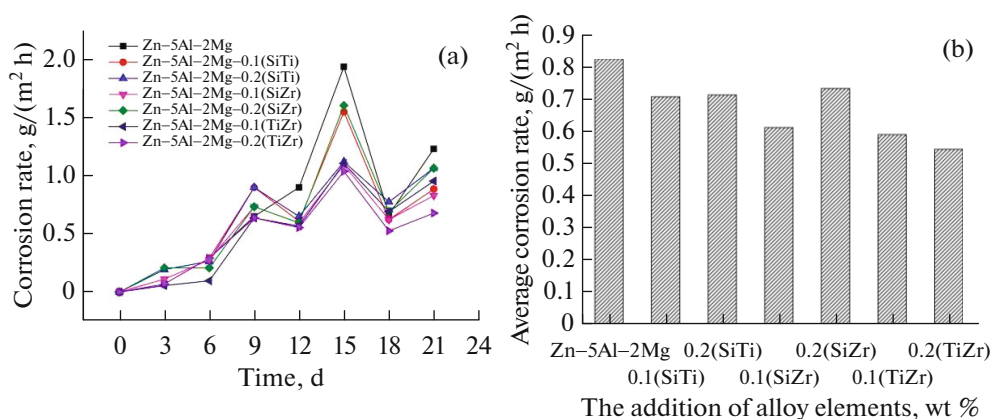


Fig. 12. Total immersion test diagram of alloys: (a) corrosion weight loss rate curves; (b) average corrosion rate histogram.

ther that the adding of Ti and Zr elements can significantly improved the corrosion resistance of the alloy.

3.6. X-ray Photoelectron Spectroscopy Analysis

In order to identify corrosion products and analyze the corrosion mechanism, the Zn-5Al-2Mg and Zn-5Al-2Mg-0.2(TiZr) alloys were tested by XPS, and the results were presented in Figs. 13 and 14. The surface corrosion products of Zn-5Al-2Mg alloy mainly contained Zn, Al, Mg, C, O and other elements in Fig. 13a. The appearance of C mainly came from the C adsorbed in the test process and the corrosion products formed in the corrosion process, the element O mainly came from the corrosion products on the sample surface, the elements Na and Cl came from the NaCl solution, and the elements Zn, Al and Mg mainly came from the alloy sample itself. Afterwards, these elements were used to fit by software, were showed in Figs. 13b-13f. The C 1s spectrum can be divided into two peaks at the binding energy of 284.90

and 288.96 eV, corresponding to C-C and O-C=O, respectively. The O 1s spectrum had a peak at the binding energy of 532.03 eV, which corresponded to surface hydroxides and oxygen containing organic adsorbates on the surface [36]. The binding energy of 1303.48 eV of Mg 1s corresponded to the corrosion

Table 4. Test results of alloys from polarization curves

Sample	Parameter	
	E_{corr} , V	I_{corr} , A/cm ²
Zn-5Al-2Mg	-1.526	2.461 E-4
0.1(SiTi)	-1.501	1.812 E-4
0.1(SiZr)	-1.446	1.923 E-4
0.1(TiZr)	-1.420	1.467 E-4
0.2(SiTi)	-1.517	4.189 E-4
0.2(SiZr)	-1.493	2.637 E-4
0.2(TiZr)	-1.416	1.176 E-4

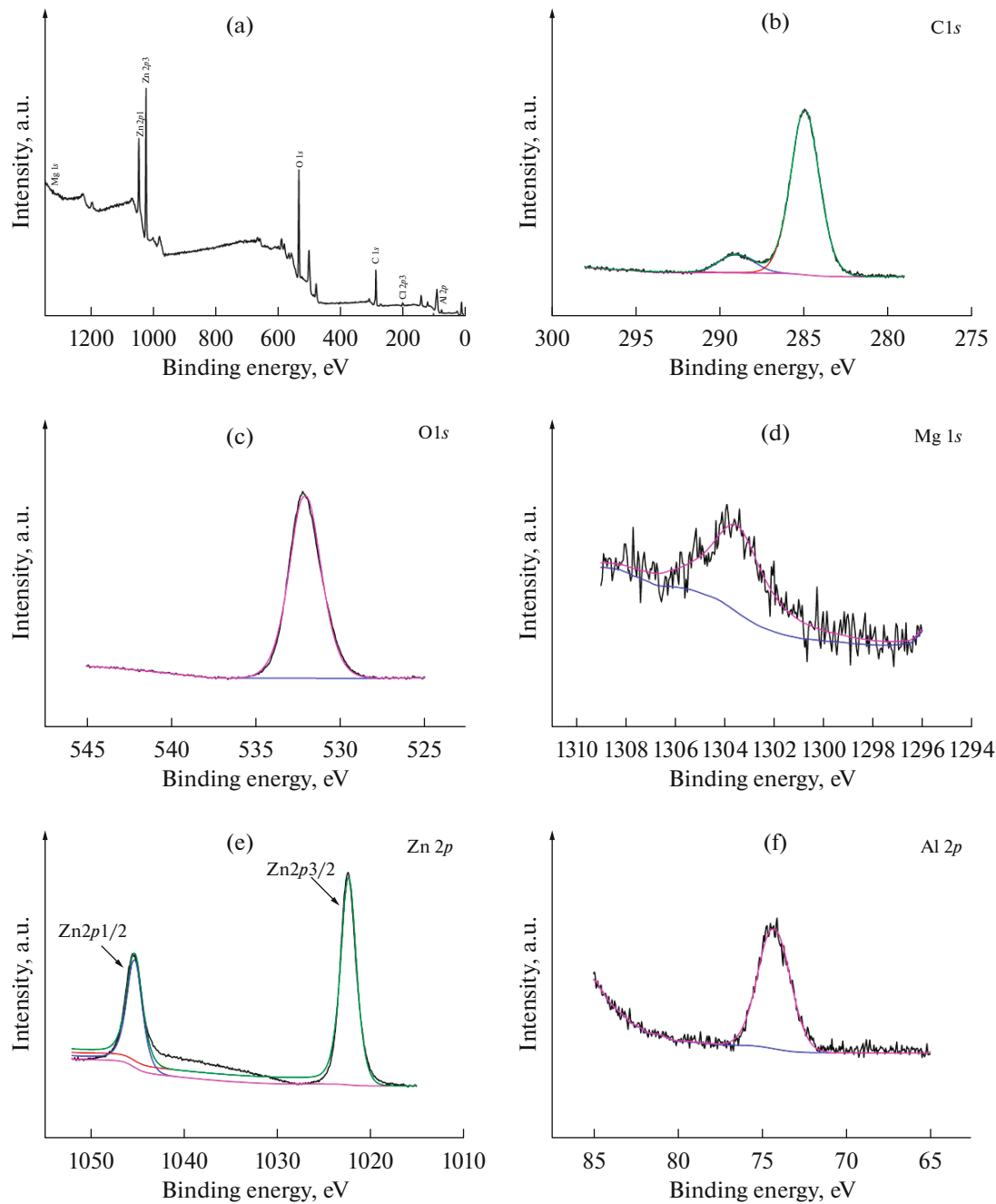


Fig. 13. XPS analysis of Zn–5Al–2Mg alloy: (a) survey spectrum; (b) C; (c) O; (d) Mg; (e) Zn; (f) Al.

product MgO, the Zn 2*p* spectrum contained two peaks, at the binding energy of 1045.11 and 1022.29 eV, all corresponded to the corrosion product ZnO. The Al 2*p* spectrum contained a peak, at the binding energy of 74.25 eV, corresponding to the corrosion product Al₂O₃ [37].

The survey spectrum of Zn–5Al–2Mg–0.2(TiZr) alloy mainly had Zn, Al, Mg, C, O and trace amounts of Ti elements, was shown in Fig. 14a. Nevertheless, Zr element was not detected and only a very small

amount of Ti was detected in the Zn–5Al–2Mg–0.2(TiZr) alloy. In addition, there was not found the corresponding compound of the Ti 2*p* spectrum at the binding energy of 476.77 and 473.98 eV in Fig. 14g. This may be due to the low content of Ti and Zr elements, or the strong corrosion resistance of Ti and Zr elements. In Figs. 14b–14f. The C 1*s* spectrum contained three peaks, at the binding energy of 284.8, 285.68 and 288.98 eV, corresponding to C–C, C–O–C and O–C=O, respectively. The binding energy of O

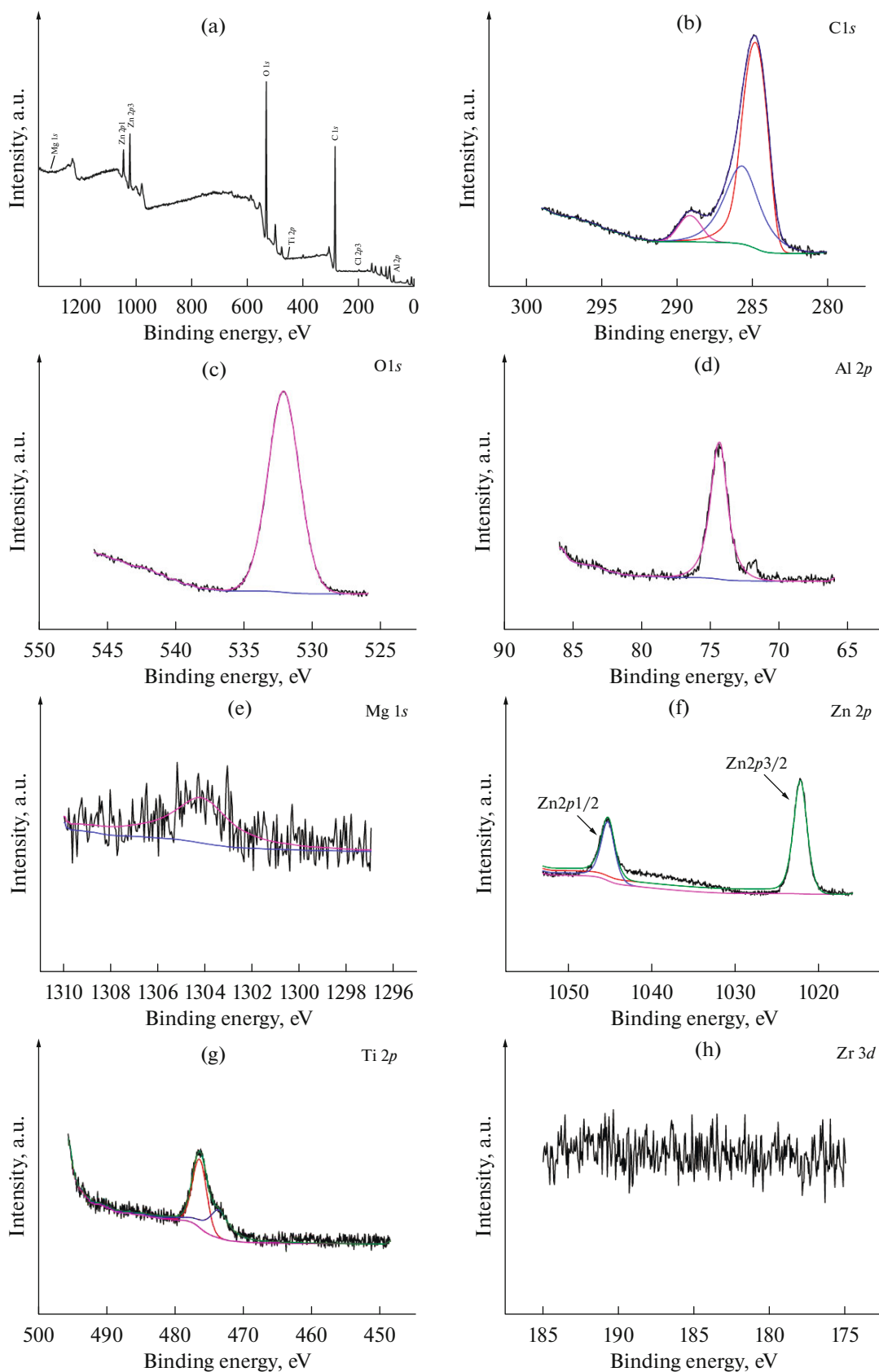


Fig. 14. XPS analysis of Zn-5Al-2Mg-0.2(TiZr) alloy: (a) survey spectrum; (b) C; (c) O; (d) Mg; (e) Zn; (f) Al; (g) Ti; (h) Zr.

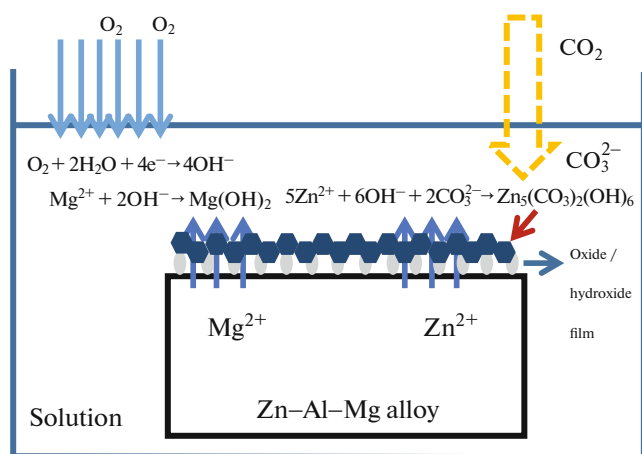
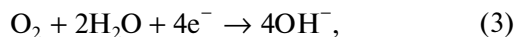
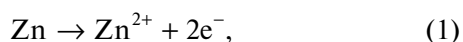


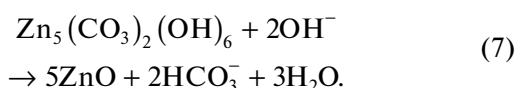
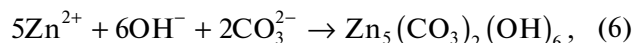
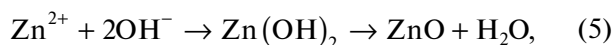
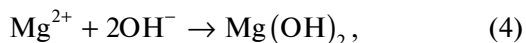
Fig. 15. The schematic model of corrosion mechanism of Zn-5Al-2Mg-z(TiZr) alloy.

1s corresponded to oxide. The binding energy of 1304.12 eV of Mg 1s corresponded to Mg^{2+} , indicating that there was $Mg(OH)_2$ in the corrosion product layer. Al element mainly existed in the form of Al_2O_3 , Zn element mainly existed in the form of $Zn_5(CO_3)_2(OH)_6$ [38].

Combined the above analysis, the schematic model of Zn-5Al-2Mg-z(TiZr) was shown in Fig. 15. It is known to all that the open circuit potentials of $MgZn_2$ and Zn were both low in Zn-Al-Mg alloys. Hence, they were generally used as anodes to participate in the electrode reaction. The oxygen in the air acted as the cathode to participate in the electrode reaction. The reaction equation was as follows:



Zn^{2+} and OH^{-} in the solution reacted to form $Zn(OH)_2$, while $Zn(OH)_2$ will further decomposed into ZnO. In addition, Zn^{2+} also reacted with OH^{-} and CO_3^{2-} in the solution to form $Zn_5(CO_3)_2(OH)_6$. As the reaction Eq. (3) progresses, the pH value increased, ZnO can originate from previously precipitated $Zn_5(CO_3)_2(OH)_6$, and its reaction was as follows equation 5, 6 and 7 [28, 38, 39].



The corrosion products of Zn-5Al-2Mg alloy were ZnO, MgO and Al_2O_3 , while the corrosion products of Zn-5Al-2Mg-0.2(TiZr) alloy were $Mg(OH)_2$, Al_2O_3 and $Zn_5(CO_3)_2(OH)_6$. It is noteworthy that Zn-5Al-2Mg-0.2(TiZr) alloy did not had ZnO which was loose, porous and easy to fall off. Instead, it produced $Zn_5(CO_3)_2(OH)_6$ with better structure compactness and good adhesion [40]. The reason that may be the addition of Ti and Zr elements, promoted the formation of $Zn_5(CO_3)_2(OH)_6$, inhibited the formation of ZnO and the progress of reaction Eq. (7). $Zn_5(CO_3)_2(OH)_6$ can adhere to the surface of the sample to form a viscous protective layer, which hindered the transfer of electric charges, thereby reduced the corrosion rate of the sample to a certain extent.

CONCLUSIONS

The effects of the addition of Si, Ti and Zr elements to the Zn-5Al-2Mg alloy on the microstructure and corrosion resistance were studied. Major conclusions drawn from the work were summarized below:

(1) The Zn-5Al-2Mg alloy mainly contained Zn phase, Al phase and Zn/Al/Mg Zn_2 ternary eutectic structure. When Si, Ti and Zr were added in binary and equal proportion respectively, Si rich phase, $Ti(Al_{1-x}Si_x)_3$ phase, Al_3Zr phase and $Al_3(Ti, Zr)$ phase appeared in the alloys.

(2) The Rockwell hardness value of these alloys by the addition of Si, Ti and Zr elements were higher than Zn-5Al-2Mg alloy. Among these alloys, Zn-5Al-2Mg-0.1(SiTi) alloy had the highest hardness, reached to 79.95 HRB.

(3) Combined with the results and analyses of EIS and total immersion test, the corrosion rate of the alloy was: Zn-5Al-2Mg alloy > Zn-5Al-2Mg-(SiTi) alloy > Zn-5Al-2Mg-(SiZr) alloy > Zn-5Al-2Mg-(TiZr) alloy. The corrosion resistance of Zn-5Al-2Mg-0.2(TiZr) alloy was best in the middle of these alloys.

(4) The results of XPS showed that the corrosion products of Zn-5Al-2Mg alloy were ZnO, MgO and Al_2O_3 , while the corrosion products of Zn-5Al-2Mg-0.2(TiZr) alloy included Al_2O_3 , $Mg(OH)_2$ and $Zn_5(CO_3)_2(OH)_6$. The addition of Ti and Zr promoted the formation of $Zn_5(CO_3)_2(OH)_6$ and hindered the formation of loose, porous and easy to fall off ZnO. $Zn_5(CO_3)_2(OH)_6$ can adhere to the surface of the sample, which hindered the transfer of electric charges, thereby reduced the corrosion rate of the sample to a certain extent.

FUNDING

The financial support for this study is provided by The Natural Science Foundation of Shandong Province, China (no. ZR2021ME191).

CONFLICT OF INTEREST

The authors declare that they have no conflicts of interest.

REFERENCES

- Amadeh, A., Pahlevani, B., and Heshmati-Manesh, S., *Corros. Sci.*, 2002, vol. 44, p. 2321.
- Shibli, S., Meena, B.N., and Remya, R., *Surf. Coat. Technol.*, 2015, vol. 262, p. 210.
- Ding, C.F., Ma, Z., Liu, S.W., Zhao, J.H., Luo, Q., Liu, H.L., Wu, G.X., and Zhang, J.Y., *Mater. Charact.*, 2022, vol. 185, p. 111746.
- Lin, Y.Z., *Concise Reader on Metal Corrosion and Protection*, Beijing: Chemical Industry Press, 2019.
- Padilla, V., Ghods, P., and Alfantazi, A., *Constr. Build. Mater.*, 2013, vol. 40, p. 908.
- Vagge, S.T., Raja, V.S., and Narayanan, R.G., *Appl. Surf. Sci.*, 2007, vol. 253, p. 8415.
- Thomas, S., Cole, I.S., and Birbilis, N., *J. Electrochem. Soc.*, 2013, vol. 160, p. C59.
- Yao, C.Z., Lv, H.B., Zhu, T.P., Zheng, W.G., Yuan, X.D., and Gao, W., *J. Alloys Compd.*, 2016, vol. 670, p. 239.
- Komatsu, A., Tsujimura, T., and Watanabe, K., EPO Patent EP0905270, 1999.
- Schuerz, S., Fleischanderl, M., Luckeneder, G.H., Preis, K., Haunxchmied, T., Mori, G., and Kneissl, A.C., *Corros. Sci.*, 2009, vol. 51, p. 2355.
- Li, S.W., Gao, B., Yin, S.H., Tu, G.F., Zhu, G.L., Sun, S.C., and Zhu, X.P., *Appl. Surf. Sci.*, 2015, vol. 357, p. 2004.
- Morimoto, Y., Honda, K., Nishimura, K., Tanaka, S., and Kurosaki, M., *Nippon Steel Tech. Rep.*, 2003, vol. 87, p. 22.
- Ueda, K., Takahashi, A., and Kubo, Y., *Metall. Ital.*, 2013, vol. 104, p. 13.
- Yang, S., Su, X.P., Wang, J.H., Yin, F.C., Tu, H., and Peng, H.P., *J. Alloys Compd.*, 2010, vol. 499, p. 194.
- Peng, W., Du, Q., Wu, G., Dan, W., Hu, W., and Zhang, J., *Surf. Coat. Technol.*, 2016, vol. 299, p. 56.
- Xu, X.J., Jin, X.P., Liu, Z., Zhang, B., Zhang, R.K., Zhang, Y., Zhang, P., and Wei, H.B., *Mater. Res. Express*, 2019, vol. 6, p. 1265h8.
- Liu, Z.L., Liu, X.Q., Wang, H.T., Hu, J.D., and Hou, Z.G., *J. Chin. Soc. Corros. Prot.*, 2014, vol. 34, p. 515.
- Chai, W.R., Chen, J.C., Liu, S.D., Ye, L.Y., Lin, H.Q., and Zhang, X.M., *Chin. J. Mater. Res.*, 2019, vol. 33, p. 488.
- Zhou, W., Yu, H., Li, Y.Z., Hou, J.X., Sheng, M.Q., and Xu, O.Y., *Electroplat. Finish.*, 2016, vol. 35, p. 686.
- Tong, G., Li, P., Li, Y., and Liu, X.F., *J. Alloys Compd.*, 2011, vol. 509, p. 8013.
- Prosek, T., Hagstrom, J., Persson, D., Fuertes, N., Lindberg, F., Chocholaty, O., Taxén, C., Serák, J., and Thierry, D., *Corros. Sci.*, 2016, vol. 110, p. 71.
- Yu, A.W., Yang, C.G., Liu, F.C., Zheng, Q., Liao, Y.F., and Chen, H., *Rare Met. Mater. Eng.*, 2015, vol. 44, p. 1964.
- Liu, W.S., Huang, B.Y., Tang, J.C., Zhou, K.C., He, Y.H., and Liu, Y., *Chin. J. Nonferrous Met.*, 2003, vol. 13, p. 153.
- Jain, D., Pareek, S., Agarwala, A., Shrivastava, R., Sassi, W., Parida, S.K., and Behera, D., *J. Mater. Res. Technol.*, 2020, vol. 10, p. 738.
- Ma, Y.L., Xiong, H.W., and Chen, B.Y., *Corros. Sci.*, 2021, vol. 191, p. 109759.
- Zhao, M.C., Liu, M., Song, G.L., and Atrens, A., *Corros. Sci.*, 2008, vol. 50, p. 3168.
- Jiang, Q., Miao, Q., Liang, W.P., Ying, F., Tong, F., Xu, Y., Ren, B.L., Yao, Z.J., and Zhang, P.Z., *Electrochim. Acta*, 2014, vol. 115, p. 644.
- Peng, S., Xie, S.K., Xiao, F., and Lu, J.T., *Corros. Sci.*, 2019, vol. 163, p. 108237.
- Ribeiro, D.V. and Abrantes, J., *Constr. Build. Mater.*, 2016, vol. 111, p. 98.
- Zhang, M.M., Zhou, G.R., Sun, H.J., Teng, X.Y., and Zhao, Z.L., *Mater. Corros.*, 2020, vol. 71, p. 1.
- Yadav, A.P., Nishikata, A., and Tsuru, T., *Br. Corros. J.*, 2008, vol. 43, p. 23.
- Xian, Z., Leygraf, C., and Wallinder, I.O., *Corros. Sci.*, 2013, vol. 73, p. 62.
- Asgari, H., Toroghinejad, M.R., and Golozar, M.A., *Appl. Surf. Sci.*, 2007, vol. 253, p. 6769.
- Xu, W.C., Fan, H.Q., Zhao, T.L., Zhang, Z.H., Liu, Y.B., and Li, Q., *Chin. J. Nonferrous Met.*, 2020, vol. 30, p. 1378.
- Uchida, Y. and Yamakawa, K., *Tetsu to Hagane*, 1995, vol. 81, p. 995.
- Pohl, K., Otte, J., Thissen, P., Giza, M., Maxisch, M., Schuhmacher, B., and Grundmeier, G., *Surf. Coat. Technol.*, 2013, vol. 218, p. 99.
- Huang, X., Wang, L.T., Song, Y.F., Ge, F., Zhang, Y., Meng, X.J., Ge, H.H., and Zhao, Y.Z., *J. Alloys Compd.*, 2021, vol. 874, p. 159807.
- Huang, Q., Wang, Y., Zhou, B., Wei, Y.Z., Gao, F., and Fujita, T., *Corros. Sci.*, 2021, vol. 179, p. 109165.
- Azevedo, M.S., Allely, C., Ogle, K., and Volovitch, P., *Corros. Sci.*, 2015, vol. 90, p. 472.
- Gao, P., *Study on the Corrosion Properties of Zn6Al3Mg Alloys and Zn11Al3Mg Alloys*, China University of Mining and Technology, 2018.